Virtual-tissue computer simulations define the roles of cell adhesion and proliferation in the onset of kidney cystic disease

Julio M. Belmonte[a,†,*], Sherry G. Clendenon[a,†], Guilherme M. Oliveira[a,†], Maciej H. Swat[a], Evan V. Greene[b], Srividhya Jeyaraman[a], James A. Glazier[a], and Robert L. Bacallao[b,*]
[a]Biocomplexity Institute, Physics Department, Indiana University, Bloomington, IN 47405; [b]Division of Nephrology, Richard L. Roudebush VA Medical Center, and Indiana University School of Medicine, Indianapolis, IN 46202

ABSTRACT **In autosomal dominant polycystic kidney disease (ADPKD), cysts accumulate and progressively impair renal function. Mutations in PKD1 and PKD2 genes are causally linked to ADPKD, but how these mutations drive cell behaviors that underlie ADPKD pathogenesis is unknown. Human ADPKD cysts frequently express cadherin-8 (cad8), and expression of cad8 ectopically in vitro suffices to initiate cystogenesis. To explore cell behavioral mechanisms of cad8-driven cyst initiation, we developed a virtual-tissue computer model. Our simulations predicted that either reduced cell–cell adhesion or reduced contact inhibition of proliferation triggers cyst induction. To reproduce the full range of cyst morphologies observed in vivo, changes in both cell adhesion and proliferation are required. However, only loss-of-adhesion simulations produced morphologies matching in vitro cad8-induced cysts. Conversely, the saccular cysts described by others arise predominantly by decreased contact inhibition, that is, increased proliferation. In vitro experiments confirmed that cell–cell adhesion was reduced and proliferation was increased by ectopic cad8 expression. We conclude that adhesion loss due to cadherin type switching in ADPKD suffices to drive cystogenesis. Thus, control of cadherin type switching provides a new target for therapeutic intervention.**

Monitoring Editor
Leah Edelstein-Keshet
University of British Columbia

Received: Feb 16, 2016
Revised: May 10, 2016
Accepted: May 10, 2016

INTRODUCTION

Autosomal dominant polycystic kidney disease (ADPKD) is the most prevalent monogenetic cause of kidney failure in the United States. The only therapeutic options for ADPKD patients are lifetime dialysis or renal transplantation. Almost all ADPKD cases are related to mutations in PKD1 (85%) or PKD2 (15%) genes, which encode transmembrane proteins polycystin-1 (PC-1) and polycystin-2, respectively (Wilson, 2004). PKD mutations impair multiple signaling pathways that affect growth and differentiation of renal epithelial cells, including those for cAMP, mammalian target of rapamycin, epithelial growth factor receptor, and jak/stat (Calvet, 1993; Gallagher *et al.*, 2002; Harris and Torres, 2009; Fedeles *et al.*, 2014). How PKD mutations effect these signaling changes is not clear, but disruptions of ciliary and planar cell polarity signaling are strongly implicated (Menezes *et al.*, 2004; Bacallao and McNeill, 2009; McNeill and McNeill, 2009). Primary cilia transduce a complex pool of external stimuli to intracellular signaling pathways that in turn control cellular functions (Kathem *et al.*, 2014).

Multiple lines of evidence indicate that ADPKD initiation also involves dysregulation of cell–cell adhesion. In ADPKD, annexin 5 forms a complex with PC-1 that disrupts E-cadherin assembly in the basolateral membrane of renal epithelial cells (Markoff *et al.*, 2007), and primary cultured renal epithelial cells derived from ADPKD kidneys fail to assemble E-cadherin stably (Charron *et al.*, 2000b). In normal renal epithelial cells, PC-1 and E-cadherin form a complex at

This article was published online ahead of print in MBoC in Press (http://www.molbiolcell.org/cgi/doi/10.1091/mbc.E16-01-0059) on May 18, 2016.

†These authors contributed equally to this work.

J.M.B., S.G.C, J.A.G., and R.L.B. conceptualized the study and designed the experiments. J.M.B. developed the in silico virtual-tissue model. J.M.B. and G.M.O. conducted the in silico simulations and their quantitative analysis. J.S. developed the phenomenological description of contact inhibition of proliferation. S.G.C., E.V.G., and R.L.B. conducted and analyzed biological experiments and provided biological context for development of the in silico work. J.M.B., S.G.C., M.H.S., J.A.G., and R.L.B. wrote the manuscript.

*Address correspondence to: Robert L. Bacallao (rbacalla@iu.edu), Julio M. Belmonte (jmbelmon@indiana.edu).

Abbreviations used: ADPKD, autosomal dominant polycystic kidney disease; cad8, cadherin-8; CC3D, CompuCell 3D; ECM, extracellular matrix; HK, human kidney; HmPKD1, human polycystin-1 gene; HmPKD2, human polycystin-2 gene; MDCK, Madin–Darby canine kidney; MOI, multiplicity of infection; PC-1, polycystin-1; TC, target cell; TTA, tet transactivator; VT, virtual tissue; WT, wild type.

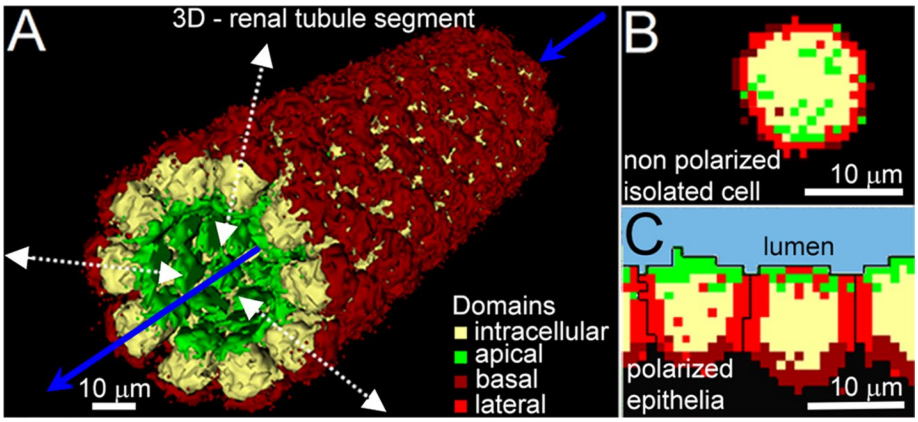

FIGURE 1: Renal tubule segment and renal epithelial cell models. (A–C) Epithelial cells have four compartments representing basal (dark red), apical (green), lateral (red), and cytoplasmic (yellow) regions. Transparent black represents ECM. Light blue represents lumen in C. (A) 3D renal tubule segment model. Dashed white arrows represent transport across the epithelial layer, and solid blue arrows represent fluid flow through the tubule lumen. Lateral (red) compartments and lumenal fluid are not shown in the 3D tubule rendering. (B) Without external cell–substrate or cell–cell binding cues, surface compartments representing adhesion molecules randomly distribute near the cell surface. (C) When renal epithelial cells contact other cells, lumen, or ECM, the cell surface domains arrange themselves according to their adhesive affinities, creating ordered apical, basal, and lateral domains.

the adherens junction, whereas in ADPKD cystic cells, both PC-1 and E-cadherin remain cytoplasmic (Roitbak *et al.*, 2004). Profound changes in cadherin expression and localization accompany cell dedifferentiation in ADPKD (Supplemental Table S1). Of note, cadherin-8 (cad8), a type II cadherin present in developing and absent in adult kidneys, is detected in 40% of cysts in ADPKD. Focal introduction of cad8-expressing adenovirus into in vitro cystogenesis culture sufficed to initiate cyst development at target sites (Kher *et al.*, 2011), and the morphology of the in vitro cysts closely resembled simple renal cysts seen in microdissections of human nephrons (Baert, 1978). All cells in induced in vitro cysts expressed cad8, whereas few cad8-expressing cells were found in the adjacent tubule (Kher *et al.*, 2011; see later discussion of Figure 3C).

In this article, we examine two hypothetical cell-level mechanisms by which abnormal expression of cad8 could initiate cyst formation: 1) reduction of cell–cell adhesion, which then leads to changes in proliferation, or 2) direct reduction of contact inhibition of proliferation with no change in cell–cell adhesion. To test these mechanisms, we built a three-dimensional (3D) virtual-tissue (VT) computer model of the renal tubule using the CompuCell3D (CC3D) modeling environment (Swat *et al.*, 2012). Our VT simulations predicted that either mechanism could initiate cyst formation, but only loss-of-adhesion simulations produced morphologies matching in vitro cad8-induced cysts.

RESULTS

Virtual-tissue model of renal epithelial cells and tubules

The nephron—the basic morphological and functional unit of the kidney—is composed of a renal corpuscle, which filters blood plasma, and a renal tubule, which reabsorbs plasma filtrate and concentrates waste for excretion. Our VT model conceptualizes a renal tubule as a series of cylindrical segments (Figure 1A). We initialize our tubule segment model in CC3D as a 15-cell-long simple epithelial tubule with a circumference of 10 cells enclosing a fluid-filled lumen within extracellular matrix (ECM; Figure 1 and Supplemental Movie S1). Apical cell domains contact fluid-filled lumen, and basal cell domains—the external surface of the tubule—contact ECM. We assume that for each tubule segment, regardless of position in the nephron, fluxes across the tubule segment epithelial layer (dashed white arrows in Figure 1A) and flow through the tubule segment (solid blue arrows in Figure 1A) are in balance such that lumen pressure and thus tubule diameter remain constant (Supplemental Movie S7). This assumption is consistent with stop-flow measurements of fluid flow through the tubule, in which lumen size was observed to vary <10% under normal physiological conditions (Brunner *et al.*, 1966).

To model tissue scale events, we use the Glazier–Graner–Hogeweg/cellular Potts model (GGH/CPM; Glazier and Graner, 1993; Swat *et al.*, 2009, 2012). Our in silico renal epithelial cells have compartments representing the segregated surface regions (lateral, apical, and basal) and an intracellular compartment representing cytosol and nucleus (Figure 1 and Supplemental Figures S2 and S3). Adhesion properties of each voxel correspond to net adhesivity between the adhesion molecules represented in that voxel and those represented by any neighboring cellular or noncellular voxels. Thus adhesion between two cells depends on both adhesion per voxel between the cells and number of each type of voxel in each cell. Adhesion-driven segregation of cell surface molecules drives formation and maintenance of epithelia, and in the absence of cell–cell or cell–matrix contact, surface compartments remain randomly distributed (Figure 1, B and C, and Supplemental Movie S3A), as occurs in isolated cells (Roitbak *et al.*, 2004; Roignot *et al.*, 2013). Our model represents formation and maintenance of epithelia using dynamic localization and segregation of voxels of cell surface compartments guided by interaction with adjacent cells and the extracellular environment. The GGH/CPM represents cells and other simulated objects as extended domains of sites (voxels) on a regular cell lattice. We provide a brief introduction here. For more detailed information about the GGH/CPM, see Glazier and Graner (1993), and Swat *et al.* (2009, 2012).

Each lattice site has at least two attributes: its spatial location in the lattice, $\vec{i}$, and an *object* or *domain index*, σ, which specifies which *object*, or *domain*, occupies the lattice site. The object/domain σ is the set of all cell-lattice sites that share the domain index σ. A GGH/CPM *domain* may represent a biological cell, a subcellular compartment, a cluster of cells, or a portion of noncellular material, fluid or medium. The *type index*, $\tau(\sigma)$, indicates the type of object a domain represents. Whereas each object/domain has a unique σ, many objects may share the same type index τ. For example, every simulated cell has a unique σ, but all cells of the same type share a type index τ.

An *effective energy*, or cost function (*H*), is a phenomenological shorthand that expresses the properties, behaviors, and interactions of all objects/domains in the lattice and determines the sequence of domain-index copies. For example in a typical GGH/CPM model, each domain represents a call with a target volume, and domains interact with neighboring domains via contact adhesion and/or repulsion, so *H* is given by

$$H = \overbrace{\sum_{\substack{\vec{i},\vec{j} \\ \text{neighbors}}} J\left(\tau(\sigma_{\vec{i}}),\tau(\sigma_{\vec{j}})\right)}^{\text{contact energy}} + \overbrace{\sum_{\sigma} \lambda_{\text{volume}}(\sigma)\cdot[v(\sigma)-V_t(\sigma)]^2}^{\text{volume constraint}} \qquad (1)$$

The left-hand sum in Eq. 1, over all pairs of neighboring cell-lattice sites $\vec{i}$ and $\vec{j}$, calculates the *contact energy* between all pairs of neighboring domains/cells $\sigma_{\vec{i}}$ and $\sigma_{\vec{j}}$. Here $J(\tau(\sigma_{\vec{i}}),\tau(\sigma_{\vec{j}}))$ specifies the boundary energy per unit contact area for domains/cells of types $\tau(\sigma_{\vec{i}})$ and $\tau(\sigma_{\vec{j}})$ if $\sigma_{\vec{i}} \neq \sigma_{\vec{j}}$ and is 0 if $\sigma_{\vec{i}} = \sigma_{\vec{j}}$. Neighboring sites within the same domain are assumed to have zero contact energy. We specify $J(\tau(\sigma_{\vec{i}}),\tau(\sigma_{\vec{j}}))$ as a matrix indexed by the domain types. Higher (more positive) $J(\tau(\sigma_{\vec{i}}),\tau(\sigma_{\vec{j}}))$ result in greater repulsion, and lower (more negative) $J(\tau(\sigma_{\vec{i}}),\tau(\sigma_{\vec{j}}))$ result in greater adhesion.

The right-hand sum in Eq. 1, over all domains/cells, enforces an elastic volume constraint on the objects/domains. Deviations of the actual volume, $V(\sigma)$, of domain σ from its target value, $V(\sigma)$, increase the effective energy. For positive $J(\tau(\sigma_{\vec{i}}),\tau(\sigma_{\vec{j}}))$, a domain/cell has an actual volume slightly smaller than its target volume due to its surface tensions. The λ_{volume} parameter behaves like a Young's modulus, with higher values reducing the magnitude of fluctuations of a domain's volume about its target value.

Objects/domains move through sequential stochastic domain-index copy attempts that represent a simplified form of cell motility. At each step, a domain index $\sigma_{\vec{i}}$ at a randomly chosen lattice site $\vec{i}$ attempts to overwrite a neighboring lattice site, $\vec{j}$, which originally belongs to a different domain (i.e., $\sigma_{\vec{i}} \neq \sigma_{\vec{j}}$). The modified Metropolis algorithm sets $\sigma_{\vec{i}} = \sigma_{\vec{j}}$ with probability $P(\sigma_{\vec{i}} \rightarrow \sigma_{\vec{j}})$ given by the Boltzmann acceptance function:

$$P\left(\sigma_{\vec{i}} \rightarrow \sigma_{\vec{j}}\right) = \begin{cases} 1, & \Delta H \leq 0 \\ e^{-\frac{\Delta H}{T_m}}, & \Delta H > 0 \end{cases} \quad (2)$$

where ΔH is the change in the effective energy (Eq. 1) if the copy occurs and T_m specifies the amplitude of object fluctuations. By definition, copies between cell-lattice sites with the same domain index would not change the cell-lattice configuration.

Contact inhibition of proliferation regulates cell density in epithelia (Martz and Steinberg, 1972). In our model, we define the cell contact fraction α to be the cell's surface area that is in contact with other cells, $S_{contact}$, divided by the cell's total surface area, S_{total}:

$$\alpha = \frac{S_{contact}}{S_{total}} \quad (3)$$

with $0 \leq \alpha \leq 1$. We then model contact inhibition of proliferation phenomenologically with a sigmoid relating growth rate of an epithelial cell to its contact fraction:

$$\frac{dV_t}{dt} = \kappa \frac{\alpha_c^n\left(1-\alpha^n\right)}{\alpha_c^n + \alpha^n} \quad (4)$$

where V_t is the target volume of the cell (i.e., the sum of the target volumes of the cell's compartments), κ is the maximum growth rate, α_c is the critical contact fraction for growth inhibition, and n is a Hill coefficient. The result of Eq. 4 is that for given values of cell–cell adhesivity α_c and fractional volume of lateral cell compartment, as a tubule or cyst increases in radius, the contact area fraction α increases such that cells grow and proliferate, increasing the radius until α approaches α_c (Supplemental Movie S4). As a cell's target volume grows, we increase the target volume of each compartment (apical, basal, lateral, and cytosol) proportionally. We set the critical contact fraction α_c (Eq. 4) so that wild-type cells in the tubule remain contact inhibited and maintain tubule homeostasis (Supplemental Movie S4). Simulation parameters are given in Supplemental Tables S2 and S3.

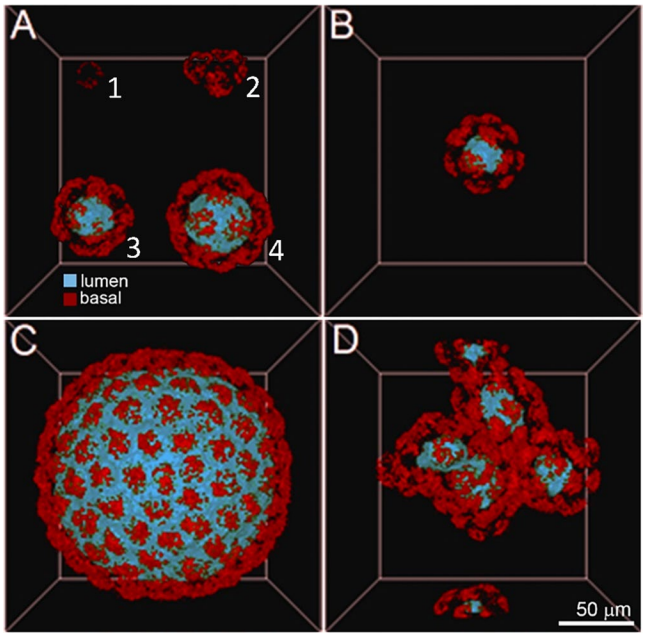

FIGURE 2: Simulated cyst formation from single isolated cells. (A–D) Cyst formation simulations starting from a single isolated cell. (A) Snapshots of reference cyst formation corresponding to 12 (1), 19.1 (2), 47.6 (3), and 142.9 (4) h. (B–D) Snapshots taken corresponding to 235.8 h, producing a (B) small-cyst phenotype, (C) large-cyst phenotype, and (D) complex multiple-cyst phenotype. Supplemental Table S2 gives a complete list of simulation parameters. Supplemental Table S4 gives a list of parameter values that produce each morphology. Lumen shown in blue, basal compartment shown in dark red; all other cell compartments were made transparent to enhance the visibility of basal compartment and lumen.

To simulate apical–basal cleavage plane polarization (Nakajima *et al.*, 2013), we specify our cleavage plane as perpendicular to the plane of the epithelium (Supplemental Movie S6). Because we do not impose planar polarity, cleavage orientation is random with respect to the tubule axis. Simulated daughter cells are cells with properties identical to those of the parent cell.

Simulation of cystogenesis from an isolated cell

Our model of cyst lumen formation and size regulation follows that of Engelberg *et al.* (2011) rather than those in continuum models (Kücken *et al.*, 2008; Gin *et al.*, 2010). Cystic lumen nucleates at any location, contacting three apical compartments of cells not currently in contact with lumen. Once created, number and surface area of cells enclosing the lumen regulate lumen target volume, $V_{t\,lumen}$:

$$\frac{dV_{t\,lumen}}{dt} = \kappa_{lumen} \times \left(N_{cells} - \kappa_r \times S_{lumen}\right) \quad (5)$$

where $V_{t\ lumen}$ is the target lumen volume, N_{cells} is the number of cells in contact with the lumen, S_{lumen} is the surface area of the lumen, κ_r is a constant that defines lumen leakage and retraction, and κ_{lumen} sets the time scale of lumen growth or shrinkage. The changing lumen target volume, in turn, causes lumen volume to change in response to the changing geometry of the surrounding epithelial cells (Engelberg *et al.*, 2011).

In simulations beginning with a single isolated cell, cell proliferation leads to cyst formation (Figure 2). Depending on the balance between cell proliferation (Eq. 4) and lumen growth (Eq. 5) and relative cell–cell and cell–ECM adhesion strengths, the cyst

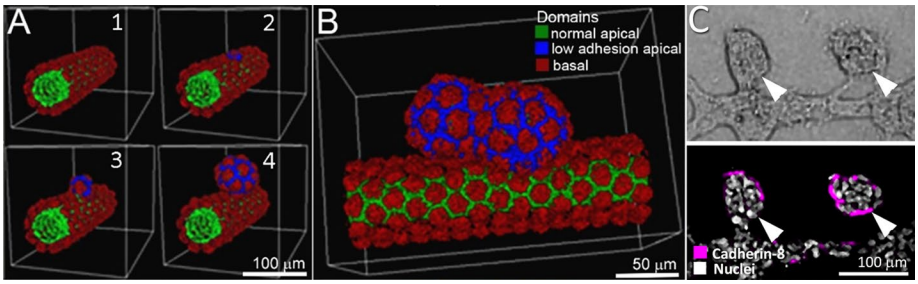

FIGURE 3: Simulations predict that cyst initiation after knock-in of cad8 is due to decreased cell–cell adhesion. (A, B) Apical compartment of WT (green), apical compartment of simulated cad8-positive TC (blue), and basal surface cells (red); other cell compartments invisible for visualization purposes. (A) Starting from a stable 3D tubular structure (1) we simulated cad8-induced cyst formation by changing the properties of a single TC (single cell with blue apical compartment; 2). Decreased adhesion between WT and simulated cad8-positive TC leads to cell protrusion into the simulated ECM (3), decreased contact inhibition, increased proliferation, and formation of an ectopic cyst from TCs only (4). (B) 3D view of a simulation run using identical parameters as in A but producing two cysts due to stochastic nature of the simulations. (C) In in vitro cultures of cysts from tubules, HK-2^{+cad8} cells are predominantly found in the forming cysts. Phase contrast image (top) and immunofluorescence images of cysts (bottom, arrows) stained for cad8 (magenta) and nuclei (white).

may remain spherical and stop growing (Figure 2B), remain spherical and grow indefinitely (Figure 2C), or split repeatedly to form multiple cysts (Figure 2D). Reference parameter values (Supplemental Table S2) result in slow cell proliferation and produce small, spherical, single-epithelial-layer cysts (Figure 2, A and B). We observed effects of varying α_c on cyst morphology. For $0.15 < \propto_c < 0.40$, cysts are spherical, with increased α_c resulting in increased cyst diameter (Supplemental Movie S7). For $\propto_c \geq 0.45$, cysts grow large, then collapse, producing multilobed cysts. Similarly, we observed effects of varying adhesion energies between lateral domains of cyst cells ($J_{TC,TC}$) on cyst morphology. For $4 < J_{TC,TC} < 20$, cysts are spherical, with increasing values of J resulting in increased cyst diameter (Supplemental Movie S7). For $J_{TC,TC} > 25$, the model produces multilobed cysts. Production of multilobed cysts is enhanced when enhanced proliferation is combined with decreased adhesion even when the parameters are within ranges that produce spherical cysts when changed individually. Lumen leakage and retraction (κ_l) also affect cyst diameter, with elevated leakage producing smaller cysts and reduced leakage producing larger cysts. These patterns of simulated isolated cyst growth closely resemble those of Madin–Darby canine kidney (MDCK) cell cysts grown in collagen culture (Figure 2; Rivers *et al.*, 1996; Engelberg *et al.*, 2011).

In vitro and virtual-tissue models for cyst initiation

In our in vitro renal tubule culture assay, we culture kidney epithelial cells under conditions that support tubule formation. We then microinject single cells in tubules with a cad8 adenovirus construct. Subsequently, over a 72-h period, cad8-expressing cysts develop at injection locations (Kher *et al.*, 2011). To match initial conditions in these experiments, our VT simulations of cad8 knock-in start with a preformed, stable tubule segment composed of normal wild-type (WT) renal epithelial cells (Figure 1). We then select one cell in the tubule as the target cell (TC) of simulated cad8 knock-in. Cadherin type switching can directly change the strength and specificity of cell–cell adhesion and can indirectly change other cell properties, such as rates of proliferation and migration (Wheelock *et al.*, 2008). In our simulations, we systematically changed cell–cell adhesion and cell proliferation to explore mechanisms of cyst initiation by ectopic expression of cad8.

Cyst initiation simulation by changes in cell–cell adhesion

In our in silico model, changes in cell–cell adhesion are linked to cell proliferation rates by a contact inhibition mechanism. Loss of contact inhibition is characterized by reduced sensitivity of cell proliferation to cell–cell contact (Martz and Steinberg, 1972). We simulate this by changing the critical ratio of cell–cell contact area, α_c, in Eq. 4. Strength of cell–cell adhesion is affected by both the strength of the specific cadherin binding and the number of cadherins present in the cell membrane (Katsamba *et al.*, 2009; Thiery *et al.*, 2012). We simulated the former by changing the adhesion energy between the cells, J, and the latter by changing the volume of the lateral surface domain, represented as the number of voxels in the lateral compartments (Supplemental Table S3).

To test whether emergent cell behaviors from changes in cell–cell adhesion can directly initiate cyst formation, we first varied TC-WT adhesion energy (Supplemental Movie S10A):

$$J(\mathrm{TC}_{\mathrm{lateral}}, \mathrm{WT}_{\mathrm{lateral}}) \neq J(\mathrm{TC}_{\mathrm{lateral}}, \mathrm{TC}_{\mathrm{lateral}}) = J(\mathrm{WT}_{\mathrm{lateral}}, \mathrm{WT}_{\mathrm{lateral}}) \quad (6)$$

Strikingly, increasing TC-WT cell–cell adhesion strength (i.e., reducing $J(\mathrm{TC}_{\mathrm{lateral}}, \mathrm{WT}_{\mathrm{lateral}})$) never induced cyst formation (Supplemental Movie S1). However, reduction of TC-WT cell–cell adhesion strength (Supplemental Table S5d) causes the TC to bulge out of the tubule plane into the simulated ECM. TC surface fraction in contact with ECM increases as the simulation continues, reducing α and thus reducing inhibition of TC proliferation (Eq. 4), resulting in cyst initiation from the tubule (Figure 3, A and B, and Supplemental Movie S2; also see later discussion of Figure 5A). Because the simulations are stochastic, the number and shape of cysts vary between simulations.

Decreasing TC-WT adhesion while leaving adhesion between target-derived cells unchanged was sufficient to initiate cyst formation. However, in vivo and in vitro, when cad8 is expressed, not only is WT-TC adhesion decreased, but TC-TC adhesion also is decreased (Supplemental Table S5e). Reducing both TC-WT and TC-TC adhesion (Supplemental Movie S10B),

$$J(\mathrm{TC}_{\mathrm{lateral}}, \mathrm{TC}_{\mathrm{lateral}}) \geq J(\mathrm{WT}_{\mathrm{lateral}}, \mathrm{TC}_{\mathrm{lateral}}) > J(\mathrm{WT}_{\mathrm{lateral}}, \mathrm{WT}_{\mathrm{lateral}}) \quad (7)$$

also led to cyst initiation. Unsurprisingly, cysts formed more readily when both were decreased than when TC-WT adhesion alone was changed.

We then simulated whether changing adhesion between cells by changing the simulated number of adhesion sites on each TC could initiate cyst formation. We changed the target volume of the lateral compartment of the TC ($V_{t\,\mathrm{lateral}}$ representing its number of adhesion sites) while maintaining the adhesion strength between lateral compartment voxels (J(lateral, lateral); Supplemental Table S5, e and f):

$$J(\mathrm{TC}_{\mathrm{lateral}}, \mathrm{WT}_{\mathrm{lateral}}) = J(\mathrm{TC}_{\mathrm{lateral}}, \mathrm{TC}_{\mathrm{lateral}}) = J(\mathrm{WT}_{\mathrm{lateral}}, \mathrm{WT}_{\mathrm{lateral}}) \quad (8)$$

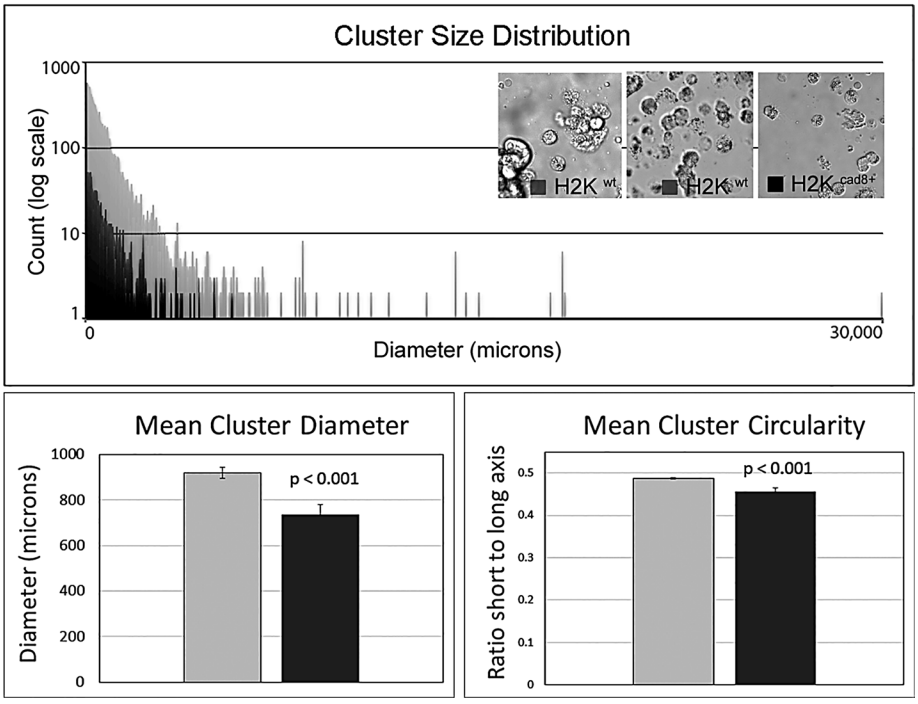

FIGURE 4: Cadherin-8 expression reduces cell–cell adhesion in HK-2 cells. Using hanging-drop assays, we compared cell–cell adhesion between HK-2 and HK-2^{+cad8} cells. Equal numbers of cells were plated in each group. Cell clusters were counted, and their diameter and circularity were quantified using FIJI ImageJ. Single cells were excluded from cluster analysis. HK-2^{+cad8} cells formed 1/10 as many clusters (HK-2, 10,758 clusters, vs. HK-2^{+cad8}, 1050 clusters). HK-2^{+cad8} cell clusters that formed were smaller and less compact than those formed by HK-2 cells (top). Insets, representative phase contrast images of hanging-drop experiments from HK-2 WT and HK-2^{+cad8} cells. Mean cluster diameter (bottom left) and circularity (bottom right) were both significantly decreased in HK-2^{+cad8} cells ($p < 0.001$).

Increasing $V_{t\,lateral}(TC) > V_{t\,lateral}(WT)$ never led to cyst formation, whereas $V_{t\,lateral}(TC) < V_{t\,lateral}(WT)/3$ supported cyst formation (Supplemental Movie S10D).

These simulation results support a mechanism by which ectopic expression of cad8 triggers cystogenesis in vivo and in vitro by decreasing adhesion between perturbed and WT renal epithelial cells through either a reduction in cadherin binding strength or a reduction in the number of cadherins on the cad8-expressing cell.

Simulations of cyst initiation by increased proliferation

In vivo, cell proliferation is infrequent in normal tubules and is increased in ADPKD (Nadasdy *et al.*, 1995b), supporting the view that renal cysts may form through increased proliferation alone (Wilson *et al.*, 1986; Chapin and Caplan, 2010). Using our VT model, we explored outcomes of directly increasing proliferation by reducing contact inhibition (by increasing values of α_c in Eq. 4; Supplemental Table S3) while holding cell–cell adhesion constant. Details of cell cycle control are not included in the model; instead, we use proliferation rates as a robust parameter to capture alterations in cell cycle transit time. Our simulations showed that this mechanism was also sufficient to generate cysts (see Figures 5B and 6C later in this article, Supplemental Movies S3, and Supplemental Figure S10C). Increased proliferation, with or without changes in cell–cell adhesion, generated cysts in silico that were composed of daughters of the TC only. No WT tubule cells were present in cysts, despite the fact that that both cell types were motile and free to mix. This emergent outcome from our in silico model simulations matched our in vitro experiments, in which cysts were formed only of human kidney-2 cells (a normal human kidney cell line) transduced with cad8 (HK-2^{cad8}; Figure 3C; Kher *et al.*, 2011).

Cadherin-8 expression reduces adhesion and increases proliferation

In our in vitro experiments, cad8 knock-in both decreased cell–cell adhesion and increased cell proliferation. We used hanging-drop assays (Kim *et al.*, 2000; Benjamin *et al.*, 2010) to measure relative cell–cell adhesion strengths of mock-transfected HK-2 and HK-2^{+cad8} cells. Note that HK-2 and HK-2^{+cad8} are the same cells as were used for our in vitro cystogenesis assays (Figure 3C). In hanging-drop assays, HK-2 cells formed tight, spherical aggregates, whereas HK-2^{+cad8} cells seldom aggregated. HK-2^{+cad8} aggregates that did form were smaller and less circular, with cells protruding from the surface and sometimes forming loosely associated sheets of cells rather than spherical clusters. These results show that HK-2^{+cad8} cells have decreased cell–cell adhesion, in agreement with our simulation predictions (Figure 4). Further, HK-2^{+cad8} cell doubling time decreased from 34.1 h for mock-transfected HK-2 cells ($N = 10$) to 23.1 h ($N = 11$, $p = 0.012$) for HK-2^{+cad8} cells. These in vitro results are in agreement with our simulations, in which decreased adhesion lowers contact inhibition, driving increased proliferation.

Simulated cyst morphologies depend on initiation mechanism

Cysts in images of isolated human nephrons (Baert and Steg, 1977) are classified as either simple cysts (see Figure 6A, inset 1, later in the article) or saccular dilations (see Figure 6A, insets 2 and 3, later in the article). Cyst height divided by cyst neck diameter, or the cyst aspect ratio, provides a simple metric to describe these morphologies in both experimental and simulation data (Supplemental Figure S8). Both loss of adhesion strength and increased proliferation due to loss of contact inhibition were sufficient to initiate cyst formation, with each simulated initiation mechanism producing a unique range of morphologies (Supplemental Table S5). When $J(WT_{lateral}, TC_{lateral}) \geq 5\ J(WT_{lateral}, WT_{lateral})$ (Figure 5A), the TC initially protrudes out into the ECM from the otherwise undisturbed tubule epithelium. TC proliferation then forms a rounded, hollow cyst outside the tubule with a narrow neck connecting the TC-composed cyst to the WT-composed tubule. This morphology matches that of cysts formed in vitro by ectopic expression of cad8 and of simple cysts in human ADPKD nephrons (Figure 6). Solely impairing contact inhibition of proliferation in TCs (by increasing α_c in Eq. 4) leads to TC proliferation, forming a patch of TCs that remains within the plane of the tubule. The patch increases in size until it evaginates, forming cysts that remain closely apposed to the tubule (Figure 5B). This morphology matches that of complex saccular dilations in human nephrons (Baert and Steg, 1977). Intermediate values of adhesion produced a range of simple cyst morphologies, whereas disruptions of contact inhibition of proliferation produced

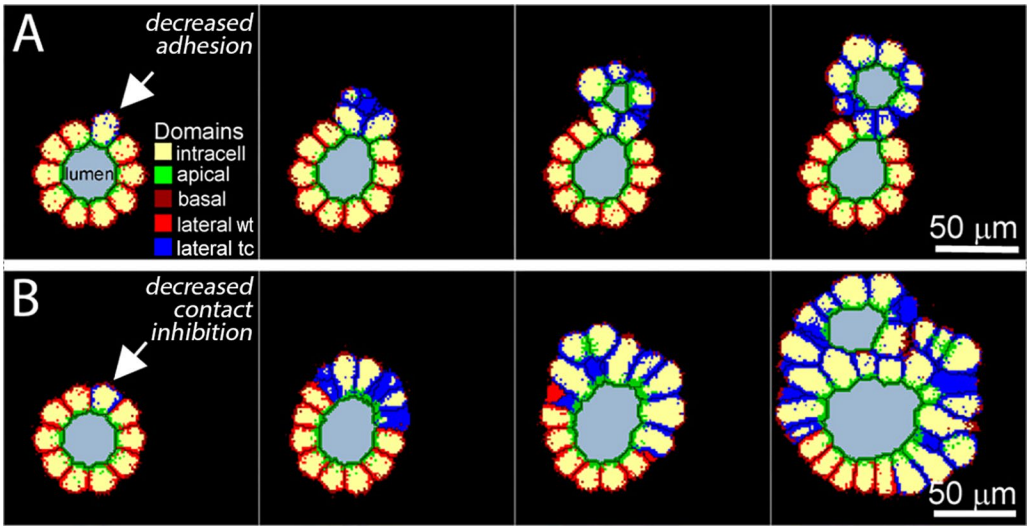

FIGURE 5: Changes in adhesion and proliferation produce distinct ranges of cyst morphology. Two-dimensional transverse slice views of 3D simulations. (A) Reduced WT-TC adhesion results in loss of contact inhibition and increased proliferation of TCs to form a cyst that grows out of the WT tubule and connects to the tubule via a narrow neck where TC and WT cells touch. (B) Increased proliferation due to decreased contact inhibition (increased α_c) in TCs while holding WT-TC adhesion constant results in lateral spread of TCs within the surface of the tubule, followed by formation of cysts that remain spread across and closely apposed to the surface of the tubule.

only saccular dilations. Growth of simulated cysts initiated by modestly increased proliferation ($\alpha_c < 0.5$) was slow (Supplemental Movie S9), similar to that seen in vivo observations in the Ift88$^{-/-}$ conditional knockout model of kidney cystic disease (Sharma *et al.*, 2013).

Modulation of simulation parameters *J*(WT, TC), *J*(TC, TC), and α_c sufficed to generate the entire range of morphologies observed in Baert's classic microdissection analysis of ADPKD nephrons, suggesting that both reduction of cell–cell adhesion and contact inhibition occur in vivo (Figure 6 and Table 1). The morphology of simulated cysts initiated by greatly reduced adhesion strength matches that of cysts formed in vitro when cell–cell adhesion is decreased by ectopic expression of cad8 and also matches that of isolated simple cysts in microdissections of human ADPKD nephrons (Figure 6 and Table 1). Thus our simulations predict, and experiments confirm, that a strong reduction in cell adhesion strength is sufficient to initiate cyst formation as seen in our in vitro cad8 cystogenesis cultures, whereas the range of cyst morphologies observed in microdissection analysis of ADPKD nephrons (Baert and Steg, 1977) can be explained only by the presence of different degrees of reduction of adhesion strength or a combination of reduced adhesion strength and direct disruption of contact inhibition of proliferation (Figure 6). Supplemental Table S5 gives a full summary of the simulation results related to changes in cell–cell adhesion and contact inhibition. These results identify at least two interdependent cell level mechanisms that result in large-scale morphological differences in the initial formation of cysts.

DISCUSSION

ADPKD is one of the first monogenetic diseases associated with defective cilia function and is one of a group of diseases called ciliopathies in which the gene products either assemble at the cilia or at the basal bodies located on the base of cilia (Gunay-Aygun, 2009). The products of the human polycystin-1 and -2 genes (HmPKD1 and HmPKD2, respectively) form a heteromeric complex in kidney epithelia monocilia in which polycystin-2 (Trp2) mediates calcium influx in response to mechanical deformation (Stayner and Zhou, 2001; Vassilev *et al.*, 2001; Wilson and Wilson, 2004). Calcium signaling can also be initiated by exosome binding to fibrocystin, another component of the heteromeric complex and the protein product of the HmARPKD gene (Rohatgi *et al.*, 2008). Contextually, this signaling can result in downstream store–operated calcium release from the rough endoplasmic reticulum (Koulen *et al.*, 2002, 2005; Aguiari *et al.*, 2003). It is the altered calcium homeostasis resulting from mutations in the HmPKD1 and HmPKD2 genes that changes the activity of Ca^{2+}-inhibitable adenylyl cyclase and Ca^{2+}-dependent phosphodiesterase (Torres and Harris, 2009). The combination of low cytosolic Ca^{2+} and elevated cAMP results in feedforward stimulation of the B-Raf/MEK/ERK pathway (Yamaguchi *et al.*, 2004). Similarly, low cytosolic Ca^{2+} decreases AKT activity, which acts to inhibit B-Raf (Yamaguchi *et al.*, 2004; Boca *et al.*, 2006). Taken together the Ca^{2+} changes in APKD cells causes an inhibition of the phosphoinositide-3-kinase/AKT pathway, which then unblocks B-Raf and is permissive for cAMP-stimulated growth (Mekahli *et al.*, 2013; Fedeles *et al.*, 2014; Harris and Torres, 2014). These findings provide the mechanistic insights into the observation that isolated cystic epithelial cells exhibit increased proliferation rates in culture (Lanoix *et al.*, 1996; Bhunia *et al.*, 2002; Wilson, 2004; Li *et al.*, 2005; Manzati *et al.*, 2005; Park *et al.*, 2007).

In addition to altered Ca^{2+} signaling, PC-1 plays a prominent role in signaling pathways that control cell–cell adhesion and planar cell polarity (Silberberg *et al.*, 2005; Fischer *et al.*, 2006; Bacallao and McNeill, 2009; McNeill, 2009). PC-1 forms a heteromeric complex with E-cadherin and β-catenin (van Adelsberg, 2000; Roitbak *et al.*, 2004; Silberberg *et al.*, 2005). In isolated cystic epithelial cells, E-cadherin is synthesized with normal kinetics but fails to stably assemble in the basolateral membrane (Charron *et al.*, 2000a). However, the same cells have β-catenin associated with N-cadherin, suggesting a limited role for the canonical Wnt signaling pathway in cystogenesis in the particular case of a single truncation mutation in HmPKD1 and an apparently normal allele (Herbert *et al.*, 2013). Using a reverse transcriptase–PCR approach to define the spectrum of type I and II cadherins expressed in cystic epithelial cells, Kher *et al.* (2011) found that cad8 was expressed in cystic epithelial cells.

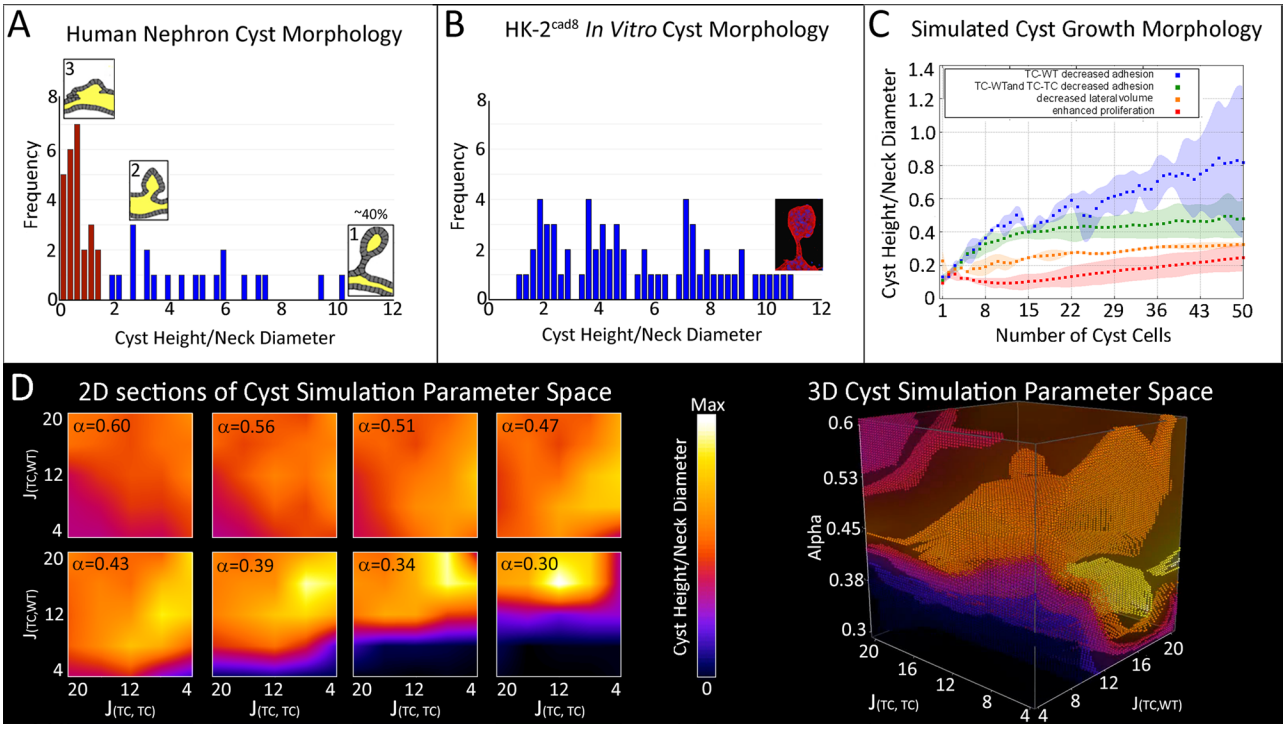

FIGURE 6: Cyst morphology in ADPKD human nephrons, HK-2^{+cad8} in vitro cysts, and virtual- tissue simulations. From images of human nephrons (Baert and Steg, 1977), images of HK-2^{+cad8} in vitro cyst cultures, and simulations, we quantified cyst morphology as the aspect ratio of cyst height to cyst neck diameter (Supplemental Movie S8). (A) Cysts in human nephrons formed two groups: 1) saccular dilations (red bars, inset 3) and 2) simple cysts (blue bars, insets 1 and 2). (B) In an in vitro cystogenesis culture system, HK-2^{+cad8} cells produced simple cyst morphology only (blue bars). Inset, an HK-2^{+cad8} cyst (red, actin; blue, nuclei). (A, B) One-way analysis of variance analysis shows a significant difference between morphology of saccular dilations (red bars in A) and simple cysts (blue bars in B) and between saccular dilations and HK-2^{+cad8} in vitro cysts (blue bars in B; both $p < 0.01$). No significant difference in morphology exists between simple cysts (blue bars in A) and HK-2^{+cad8} in vitro cysts (blue bars in B). (C) Decreased TC-WT adhesion (blue) primarily produces cysts that grow away from the tubule, as in HK-2^{+cad8} in vitro cysts and human nephron simple cysts. Decreased TC-WT and TC-TC adhesion produces cysts that grow away from the tubule (green), overlapping the low end of the decreased TC-WT adhesion range. Decreased lateral adhesion compartment size (orange) produced cyst morphology approaching that produced by decreased contact inhibition. Decreased contact inhibition (red) produced cysts resembling saccular dilations. Dotted lines, mean of simulations of each type that produced cysts (Supplemental Figure S10). Shaded areas, 1 SD. (D) Three-dimensional isosurface representation of cyst initiation morphology parameter space. Axes are $\propto_c$, J(TC, WT), and J(TC, TC). Color indicates morphology metric of cyst height over cyst neck diameter. Color scale normalized to maximum morphology metric. Black regions reflect baseline parameters where cyst formation does not occur. Yellow-white regions produced stalk-type cysts.

	Simulated cell-level mechanism due to cad8 expression in TCs			Tissue-level simulation result
		Adhesion	Contact inhibition	Cyst morphology
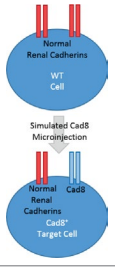	a	Cell–cell adhesion unchanged	↓	Saccular dilations
	b	↑WT-TC adhesion strength	On	No cysts
	c	↓WT-TC adhesion strength	On	Saccular dilations to simple cysts
	d	↓WT-TC adhesion strength ↓TC-TC adhesion strength	On	Saccular dilations
	e	↑TC lateral contact area	On	No cysts
	f	↓TC lateral contact area	On	Saccular dilations

See Supplemental Table S5 for additional information, including descriptions of a–f.

TABLE 1: Cyst morphology simulation outcomes related to changes in cell–cell adhesion or contact inhibition.

Normally, cad8 is expressed early in nephrogensis but is not found in adult human kidneys (Blaschke *et al.*, 2002). It is a histological marker for renal cell carcinoma and was found in 40% of renal cysts in ADPKD kidneys (Blaschke *et al.*, 2002). In a 3D culture model, transient expression of cad8 in HK cells grown in tubule arrays was sufficient to induce cyst formation (Kher *et al.*, 2011). By controlling cad8 expression with a tet promoter, the number of cysts formed was controlled by doxycycline, confirming the role of cad8 in initiating cyst formation (Kher *et al.*, 2011). Although this study underscored the role of cell–cell adhesion in cyst formation, the mechanism of cyst formation was not elucidated. This shortcoming is a systemic problem. Typically, gene knockout studies are performed with cyst formation used as the readout for an effect. In our studies, we were able to model two cell parameters to evaluate their effect on cyst emergence: cell proliferation and cell–cell adhesion.

Of note, in our tissue simulations, increased cell proliferation is predicted to have unanticipated effects on cyst emergence and morphology. At the upper levels of the proliferative parameter space, high proliferative rates do not support cyst formation. Where the change in proliferation is determined by a loss of contact inhibition, cyst emergence starts within the plane of the tubule and then rises as a cell plaque from the tubule. The resultant cyst eventually arises largely separated from the tubule. Finally, at lower levels of proliferation occurring with decreased cell adhesion, cyst emergence is characterized by cell migration away from the tubule, resulting in a stalk attached to the cyst (Figure 5). The tissue model predicted that stalk morphology occurs when cystic cells have a 30% decrease in doubling time compared with normal cells, a finding confirmed experimentally. At low levels of proliferation, cyst emergence is not observed. Taking the results together, the model predicts that cyst emergence occurs only when proliferation is constrained within a defined range and is enhanced by decreased cell adhesion.

To further understand the relative roles of cell–cell adhesion and loss of contact inhibition of cell proliferation on cyst morphology, we examined the distribution of human cyst morphologies relative to parameter alterations (Figure 6). By varying adhesion strength and contact inhibition through a range of intermediate values, the contribution of the parameter class to emergent cyst morphologies can be determined. From this analysis, we confirmed that loss of contact inhibition is deterministic for saccular cyst morphology, whereas diminished cell–cell adhesion drives cyst emergence with stalk formation. Thus modeling allows full exploration of the parameter space, which cannot be matched by current experimental approaches. If transgenic approaches were used as the strategy to determine gene dosage effects on cyst morphology, studies would require extensive breeding strategies and attendant costs. In contrast, the extremes of model parameters can be used to test model predictions by looking at predicted boundary conditions by using a complete gene knockout or expressing modified functional gene products.

Despite extensive work uncovering genetic changes associated with PKD and the signaling pathways altered in the setting of PKD mutations, we do not know the precise sequence of events that leads to cyst initiation. Our combined computational and experimental results provide a mechanistic explanation for cell behaviors underlying cyst initiation in kidney cystic diseases. We hypothesize that when mutations are present in PKD-associated genes, cadherin selection is altered, resulting in focal and clonal changes in cadherins expressed by affected cells. Our VT model predicted and our experiments confirmed that changes in adhesion and contact inhibition of proliferation are then sufficient to initiate cyst formation. As experiments further explore how mutations in polycystins induce cadherin type switching, the VT model developed here provides a platform for linking subcellular networks known to be affected by polycystin mutations with those driving selection and function of junctional complex molecules to generate hypotheses that can then be validated by targeted genetic manipulation of our in vitro cystogenesis system. Our paired in silico–in vitro model system provides a powerful quantitative tool to elucidate mechanisms by which subcellular network perturbations drive human renal cyst formation. Our work shows that adhesion loss due to cadherin type switching in ADPKD suffices to drive cystogenesis and reveals cadherin type switching as a new target for therapeutic interventions. Future models will include subcellular modules that capture cell cycle details, mitotic spindle orientation, ion transport, cell matrix interactions, and metabolism. It is likely that the interplay of these subcellular processes will lead to unexpected results.

MATERIALS AND METHODS

Cell lines and cell culture

HK-2 cells were purchased from the American Type Culture Collection (Manassas, VA) and maintained in culture as previously described (Kher *et al.*, 2011). All tissue culture reagents were obtained from Thermo Fisher Scientific (Waltham, MA). Cells were maintained in culture at 37°C in a 5% CO_2 atmosphere.

3D collagen culture

Cell matrix (Wako Chemicals, Richmond, VA) was mixed with growth medium in equal proportions, and 1 ml was layered onto 60-mm Petri dishes with a glass coverslip mounted on the bottom (MatTek, Ashland, MA). Collagen matrix was allowed to set overnight, and then HK-2 cells were plated at a density of 100,000 cells/cm^2 and incubated overnight. After cells were allowed to attach, excess medium was removed, and the cells were overlayered with cell matrix and maintained in 5% CO_2, 37°C culture conditions. Cells were kept in culture for a maximum of 14 d.

Adenovirus production

Human cad8 was obtained from Invitrogen (Carlsbad, CA) and subcloned into pAdTet (Hardy *et al.*, 1997). Cadherin-8 bearing pAdTet was cotransfected into Cre8 293 cells (generously supplied by Josh Lipshutz, University of Pennsylvania, Philadelphia, PA) with Ψ5 Ad backbone (Hardy *et al.*, 1997). Adenovirus expressing tet transactivator (TTA) was supplied by Josh Lipshutz. Multiplicity of infection (MOI) was determined by performing serial dilutions and assaying cad8 expression by immunohistochemistry in MDCK TTA-expressing cells (Clontech, Mountain View, CA).

Cyst formation assay

HK-2 cells grown in 3D collagen matrix form tubules within 24 h after collagen matrix overlay. Once tubules were formed, three different experimental conditions were evaluated. Adenovirus expressing cad8 and adenovirus expressing tet TTA, or both cad8 adenovirus and TTA adenovirus were microinjected into matrix near the tubules. Typically, 1E6 MOI virus was microinjected in a region. In addition, some experiments were performed in which cad8 and TTA adenovirus were microinjected and the cells were incubated in medium supplemented with 0, 0.5, or 1 μg/ml doxycycline. After microinjection, cultures were incubated for 48–72 h. To enable visualization of cadherin localization within cystogenesis cultures, HK-2 cells were alternately transfected with plasmids bearing Flag-tagged cad8 using XFect (Sigma-Aldrich, St. Louis, MO) according to the manufacturer's directions. After transfection, cells were grown in regular medium for 24 h, passaged with trypsin-EDTA, and mixed

with an equal number of untransfected HK-2 cells and plated on collagen matrix at a density of 50,000 cells/cm^2. Four hours after plating, the cells were overlaid with collagen and maintained in culture for 24–96 h before processing for light microscopy.

Fixation and staining of 3D cyst formation assays

Collagen matrix samples were washed three times with phosphate-buffered saline (PBS) supplemented with 0.5 mM $MgCl_2$ and $CaCl_2$. Matrix cultures were treated with 1000 U/ml collagenase II (Worthington Biochemical, Freehold, NJ) for 5 min. After three washes with ice-cold PBS supplemented with 0.5 mM $MgCl_2$ and $CaCl_2$, samples were fixed for 30 min with 2% or 4% paraformaldehyde (PFA) for 30 min. Fixation reactions were quenched with 100 mM NH_4Cl dissolved in PBS. To stain samples, collagen matrix plugs were washed with PBS with 0.1% Triton X-100 (Thermo Fisher Scientific) supplemented with 5% normal donkey serum (Jackson ImmunoResearch, West Grove, PA). To visualize overall tubule and cyst morphology, samples were labeled with rhodamine–phalloidin and Hoechst 33342 (Thermo Fisher Scientific,). To determine cad8 localization within the cyst and adjacent tubule, samples were labeled with monoclonal anti-Flag (OriGene, Rockville, MD). After labeling and washes, all samples were postfixed in PFA and mounted with Fluorsave (EMD Biosciences, Darmstadt, Germany).

Fluorescence microscopy

Fluorescently labeled samples were imaged by two-photon confocal microscopy using a FluoView 1000 confocal microscope (Olympus, Tokyo, Japan). Image processing was performed using FIJI ImageJ (Schindelin *et al*., 2012).

Hanging-drop cell adhesion assay

Cell adhesion was assayed as described previously (Kim *et al*., 2000; Ehrlich *et al*., 2002; Benjamin *et al*., 2010). HK-2 cells were maintained at <50% confluence. Plasmid DNA encoding full-length human cad8 was purchased from OriGene. Lipofectamine 2000 was purchased from Thermo Fisher Scientific. All transfections were performed with Lipofectamine 2000 according to manufacturer's directions. All experiments were performed comparing paired groups of transfected to mock-transfected HK-2 cells. A suspension of single, well-dispersed cells (25,000 cells/ml) was placed in a 20-µl volume on a 35-mm Petri cover. The cells were suspended over a 2-ml volume of medium and incubated for 24 h. The lid was inverted, and one drop was placed on a coverslip. The suspension was triturated 10 times with a 20-µl pipette, and then six random fields were photographed with an inverted Nikon microscope equipped with a Spot camera (Diagnostic Imaging Solutions, Sterling Heights, MI) with a 20× phase contrast objective. Micrographs were analyzed with Image J (to assess number of cell clusters and cell cluster size and shape). Briefly, identical acquisition settings were used for all samples. We then performed background subtraction, followed by segmentation of the clusters from background, binarization of the segmented images, and then particle analysis to count the cell clusters, measure their diameters, and measure circularity. Particles the size of a single cell or smaller were excluded from analysis. All image processing was performed using identical settings.

Measurement of cell doubling time

Mock-transfected or cad8-transfected HK-2 cells were plated at a density of 20,000 cells/cm^2 and passaged to create a single-cell suspension at 24, 48, and 72 h after plating. Cells were counted using a Countess Automated Cell Counter (Thermo Fisher Scientific). Cell counting experiments were repeated 10 times for mock-transfected cells and 11 times for cad8-transfected cells. Doubling time was calculated by measuring the slope of the plot of log(number of cells) versus time and determining the $t_{1/2}$ for cell number doubling. Statistical significance was determined using Student's *t* test with significance determined at $p < 0.05$.

GGH/CPM simulations

The GGH/CPM represents a single cell as an extended domain of sites (pixels) on a regular lattice that share a common index, σ. For detailed information about the GGH/CPM, see van Adelsberg (2000), Fischer *et al.* (2006), and Swat *et al.* (2012). Detailed cyst model parameters are given in the Supplemental Text and figures. Our CC3D model repository (compucell3d.org/Models/PKD) provides computer code for execution of all simulations used in preparing this article.

Computer simulation parameters

Sufficient detail is given here such that readers can construct and implement the computational model described. Biologically based rationale is included such that readers can accept or change parameters in their implementation of the model in an informed manner.

Cadherin expression in kidney. The kidney expresses multiple cadherins in a complex spatial and developmental pattern (Supplemental Table S1). Cadherin-8 is present in normal embryonic and adult cystic kidney but absent in normal adult kidney (Kher *et al*., 2011).

Kidney tubule morphology. Our in silico tubule segment with a circumference of 10 cells enclosing a lumen replicates the typical dimensions of normal proximal and distal kidney tubules (Supplemental Movie S1).

GGH/CPM. The GGH/CPM model is briefly described in the *Results* section, and more complete descriptions can be found in Swat *et al*. (2009, 2012). Model simulations performed in support of this article focused on cell–cell adhesion and contact inhibition, and both aspects of cell behavior are iteratively calculated for each matrix point in Eq. 1.

Cell compartment models. In simple GGH/CPM models, cells are internally homogeneous. To represent subcellular spatial structure, we extend the GGH/CPM formalism (Starruß *et al*., 2007; Popławski *et al*., 2008; Scianna *et al*., 2011) and represent each biological cell as a collection of compartments identified by a *cluster index*, θ. Each compartment represents a biological subcellular unit, such as the cell membrane or nucleus (Supplemental Movie S2A) or the apical, lateral, or basal surface domain of an epithelial cell (Supplemental Movie S2B). The contact energies in the effective energy (Supplemental Eq. S1) differ if compartments belong to the same cell or different cells, such that $J(\tau(\sigma_{\vec{i}},\theta_{\vec{i}}),\tau(\sigma_{\vec{j}},\theta_{\vec{j}}),\sigma_{\vec{i}},\sigma_{\vec{j}})$. To keep cells from falling apart (Supplemental Movie S2C), adhesion between internal compartments must be stronger than between compartments of different cells (Supplemental Movie S2B). In addition, we modify the volume constraint term in Supplemental Eq. S1 to sum over all compartments in addition to all cell objects and domains.

Dynamic cell compartments model. To model emergent cell polarization and epithelialization, we allow compartments within a cell to mix, providing a coarse-grained representation of the spatial

distribution of a protein, or set of proteins, that have internal and external contact preferences. As an example, we set the contact energies between compartments within a cell and between compartments belonging to different cells to drive segregation of the compartments, emergence of cell polarity, and creation of a polarized epithelium. To represent surface domains, we choose internal adhesion energies so the compartments segregate primarily to the cell surface (plasma membrane) rather than the cell interior (cytoplasm; Supplemental Movie S3A). To represent proteins like cadherins that segregate to the cell surface and also preferentially establish homophilic links between adjacent cells, we assign relatively strong attraction between surface compartments of the same type belonging to different cells, so that they cluster at apposing cell surfaces (Supplemental Movie S3B, green voxels). Appropriate choices of contact energies between compartments in different cells can also model heterophilic receptors, such as ephrin receptor/ephrin pairs (Supplemental Movie S3C, green and blue voxels), or integrin-mediated cell–matrix attachment.

Modeling renal epithelial cells. We use the dynamic compartment model to represent renal epithelial cells. In these cells, cadherin complexes that mediate cell–cell adhesion populate the lateral surface domains, integrin complexes that mediate cell–matrix adhesion populate the basal surface domains, and apical domains reside at the interface between the cell and lumen. Simulated cells include three surface compartments—apical, basal, and lateral—and one core compartment—the cytosol—representing the inside of the cell.

As in our previously published models of epithelial cells in forming somites (Dias *et al*., 2014), we assume that a cell's environment guides the localization of its surface domains, with lateral compartments preferentially localizing to cell–cell contact interfaces and basal compartments to cell–ECM interfaces (Figure 1C). The cell–medium interface serves as a proxy for the cell–ECM interface. We set the target volumes of each surface compartment to produce a quasicuboidal epithelial cell shape, with the lateral compartment occupying 66% of the cell surface, the apical compartment occupying 14% of the cell surface, and the basal compartment 20% of the cell surface.

The dynamic compartment model allows us to simulate changes of both the strength of adhesion per simulated cadherin molecule and the number of simulated cadherins at the cell membrane. Our model simulates the first case by changing the adhesion energy per voxel between the cells (the *J* term in Eq. 1) and the second by changing the target size of the lateral compartment. Our use of a neighbor order number of 4 (Supplemental Tables S2 and S4) introduces a predicted error in adhesion energy strengths (Magno *et al*., 2015). In future models, adhesion energy strengths per voxel will be linked directly to experimentally determined values for cadherins, but our present simulation results are not affected by this theoretical error.

Modeling cell proliferation and contact inhibition. Our cyst model uses a phenomenological model of contact inhibition of cell proliferation in which the fractional area of cell–cell contact α (Eq. 3) regulates the rate of increase of the target volume of the kidney epithelial cells as in Eq. 4, which is repeated here:

$$\frac{dV_t}{dt} = \kappa \frac{\alpha_c^n \left(1-\alpha^n\right)}{\alpha_c^n + \alpha^n}$$

Here V_t is the target volume of the cell, κ is the maximum growth rate, α_c is the critical fractional area of cell–cell contact for growth inhibition, and n is a Hill coefficient. We chose a value for α_c that maintains the original WT cells on the tubule epithelial layer in a contact-inhibited state since proliferation within normal tubules is low (Nadasdy *et al*., 1994, 1995a). As can be seen in Supplemental Movie S3, even the use of Eq. 3 to calculate cell surface leaves some fluctuations around its mean value. Therefore we set a value for α_c to be less than $<\alpha> - 2$ std(α), where std(α) is the SD from the mean value of the cell–cell contact surface for the modeled epithelial cells ($<\alpha>$).

As the cell grows, we increase the target volume of each compartment (apical, basal, lateral, and cytosol) proportionately to preserve the initial volume distributions of compartments. Cells divide symmetrically when the actual cell volume reaches $2V_0$. This model neglects the complexity of noncontact modulators of cell growth, the phases of the cell cycle, and cell cycle checkpoints, assuming that all cells are intrinsically proliferative, that the rate of growth during G1 phase depends only on cell–cell contact and not on other modulators such as growth factor, nutrient, or O_2 availability, and that S, G2, and M phases are short enough compared with G1 that we can treat them as instantaneous. In subsequent implementations of this model, additional cell cycle complexity can be added if needed for comparison with experimental results.

Averaging cell surface-area fluctuations

In GGH/CPM simulations, the instantaneous surface area of a cell fluctuates widely, even when the average cell volume remains constant. Thus the fractional area of cell–cell contact (Eq. 3) and the growth rate of the cell (Eq. 4) can fluctuate rapidly in a nonbiological manner. We therefore smooth α using a moving average of the cell surface area:

$$\langle S \rangle_t = \langle S \rangle_{t-1} \times w + S \times (1-w) \qquad (S1)$$

where w is between 0 and 1 and sets the memory time in the moving average (the memory decay time is $-\frac{23.1 \pm 10.8 \text{ h}}{\ln(1-w)}$). Supplemental Movie S5 shows a time plot of smoothed cell surface area for a representative cell for different values of the smoothing parameter, w.

Orientation of cell division

A cell divides into two daughter cells along a division plane normal to the plane of the epithelium (Supplemental Movie S6, red cell). The cleavage axis is randomly oriented with respect to the tubule axis because we do not consider planar cell polarity in our simple model (Supplemental Movie S6, green cells). After division, the daughter cells depolarize and their compartments randomly redistribute across their volumes. The cells then repolarize emergently through their interactions with neighboring cells, lumen, and matrix.

A strength of computational modeling is the ability to control multiple parameters in ways that are difficult or impossible to do in biological systems. These in silico explorations of parameter space provide insight into biological mechanisms and their tissue-level outcomes. Our virtual-tissue models of cyst initiation allow us to examine multiple combinations and ranges of altered adhesion strengths and impaired contact inhibition (Supplemental Table S3). Although not all of these combinations of adhesion and contact-inhibition impairment are biologically plausible, exploring these parameter spaces in silico enables better understanding of the biological system. In ADPKD tissues, E-cadherin on the cell surface is reduced and cad8 expression is frequently atavistically turned on (Kher *et al*., 2011). Based on our experimental results (Figure 4),

these changes are expected to reduce adhesion between cystic and noncystic cells of the renal tubule and between cystic cells. This case is represented in our simulations by the reduction of both WT-TC and TC-TC adhesion (Supplemental Table S5d).

Cyst morphology quantification

We quantified cyst morphology in images of isolated human nephrons and in vitro cystogenesis cultures as a ratio of cyst height to cyst neck diameter. Cyst neck diameter was the diameter of the cyst neck at the surface of the tubule (Supplemental Figure S8B). Cyst height was the distance from the surface of the tubule to the centroid of the cyst (Supplemental Movie S8C). We calculated simulated cyst morphology also using the aspect ratio of cyst height to cyst neck diameter. We estimate cyst height as the distance between the surface of the WT tubule and the centroid of the cyst (Supplemental Movie S9F). Cyst neck diameter is calculated as the mean of the long and short axes of the cyst neck diameter (Supplemental Movie S9, D and E), calculated as the maximum linear distance between TC voxels at the surface of the WT tubule.

To determine the height of the cyst, H_c, we calculate the mean of the distances from TC centers of mass to the center of the tubule and subtract the tubule's radius:

$$\langle H_c \rangle = \frac{1}{N_{TC} + N_{lum} - 1} \sum_k \sqrt{(x_k - x_{cl})^2 + (y_k - y_{cl})^2} - r_{tub} \qquad (S2)$$

where x_k and y_k are the center-of-mass coordinates for TCs and the cyst lumen(s), x_d and y_d are the central lumen center-of mass coordinates, and r_{tub} is the tubule radius. N_{TC} and N_{lum} are, respectively, the total numbers of TCs and lumens. Note that the tubule lumen is omitted from the summation, giving the $N_{lum} - 1$ term.

We calculate the location of the center of the tubule, using the fact that the tubule is parallel to the *z*-direction. The location of the center of the tubule is then the center of mass of the *xy*-coordinates of the WT cells. Tubule radius is then calculated as the mean of the distance of all WT cell basal compartment centers of mass to the center of the tubule. To calculate cyst neck diameter, we examine all TC voxels that lie r_{tub} from the tubule center. From those, we calculate the maximum linear distance between those voxels in the *z*-direction and the module of the largest vector perpendicular to *z*. Cyst neck diameter is defined as the mean of these values.

Timing of simulated cyst initiation

We examined timing of simulated cyst onset due to 1) changes in adhesion linked to changes in proliferation or 2) reduced inhibition of proliferation without changes in adhesion. We simulated changes in adhesion by changing the adhesion energy between cells, *J*, or by changing the size of the lateral domain. We simulated changes in proliferation directly by altering the value of α_c while holding cell adhesion constant. Proliferation is contact inhibited for cells when $\alpha > \alpha_c$ (Supplemental Movie S4).

Morphologies of simulated cysts

We examined the temporal evolution of simulated cyst morphology initiated by 1) changes in adhesion linked to changes in proliferation or 2) reduced inhibition of proliferation without changes in adhesion, as described above.

A key finding is that distinct ranges of morphologies can be produced by each method of simulated cyst initiation, depending on degree of adhesion or proliferation disruption (Supplemental Table S5, Figure 6C, Supplemental Figure S10, and Supplemental Movies S1–S3). Strong levels of decreased adhesion are the only simulation condition that produced cysts with height/neck ratios within the range of Baert's simple cysts (Supplemental Movies S8A, cyst labeled C, and S2) and the HK-2^{cad8+} cystogenesis cultures of Kher *et al.* (2011; Figure 3C). Modest levels of decreased adhesion, just sufficient to release contact inhibition of proliferation, produced cysts with lower height/neck ratios that approached the range of Baert's saccular dilations (Supplemental Movie S8A, cysts labeled D). Overlapping morphology ranges were produced by decreasing only WT-TC adhesion (Supplemental Movie S10a) or decreasing both WT-TC and TC-TC adhesion (Supplemental Movie S10b), although decreasing both produced cysts with a slightly lower height/neck ratio and allowed cyst initiation at lower levels of adhesion loss. Increasing proliferation while holding adhesion constant always produced cysts with low height/neck diameter ratios that resemble Baert's saccular dilations (Supplemental Movie S10d). Decreasing adhesion by reducing the size of the lateral contact area also always produced cysts with lower height/neck diameter ratios (Supplemental Movie S10c).

Supplemental Movie S4 shows the result of a full exploration of the parameter values *J*(TC,TC), *J*(TC,WT), and α, where isosurfaces are used to define relative demarcations in cyst morphology. Black regions are areas where the parameters are set to baseline conditions and no cyst formation occurs. Yellow-white regions reflect regions in the parameter space where stalk morphology cyst growth is strongest.

Regardless of the method of simulated cyst initiation, cysts were composed of TCs only. Simulated cysts initiated by any method of reducing adhesion had larger height/neck ratios than simulated cysts initiated by direct alteration of α_c. Whether TCs remained confined to the cyst or expanded into the surface of the tubule was dependent on rate of proliferation. In cysts initiated by increased proliferation from directly altering α_c while holding cell adhesion constant, TCs spread extensively into the body of the tubule. In cysts initiated from loss of cell–cell adhesion with $J > 13$, height/neck ratios approached the range of Baert's saccular dilations, and TCs spread into the body of the tubule.

ACKNOWLEDGMENTS

We thank James Sluka for critical reading of the manuscript. We thank the Office of the Vice President of Research, Indiana University, Bloomington, for an Indiana University Collaborative Research Project Grant to R.L.B. and J.A.G. to initiate this project. National Institutes of Health/National Institute of General Medical Sciences R01 GM 076692, the Dr. Ralph and Marian Falk Research Trust, and National Institutes of Health Grant P30 DK 079312-03 further supported this project. R.L.B. is the recipient of a VA Merit Review, BX001736, and support from the Bloch family. We acquired images at the Indiana Center for Biological Microscopy, Indiana University School of Medicine, Indianapolis, IN, and at the Biocomplexity Institute, Indiana University, Bloomington, IN. Code for execution of all simulations is given at compucell3d.org/Models/PKD.

REFERENCES

Aguiari G, Campanella M, Manzati E, Pinton P, Banzi M, Moretti S, Piva R, Rizzuto R, del Senno L (2003). Expression of polycystin-1 C-terminal fragment enhances the ATP-induced Ca2+ release in human kidney cells. Biochem Biophys Res Commun 301, 657–664.

Bacallao RL, McNeill H (2009). Cystic kidney diseases and planar cell polarity signaling. Clin Genet 75, 107–117.

Baert L (1978). Hereditary polycystic kidney disease (adult form): a microdissection study of two cases at an early stage of the disease. Kidney Int 13, 519–525.

Baert L, Steg A (1977). On the pathogenesis of simple renal cysts in the adult. A microdissection study. Urol Res 5, 103–108.
Benjamin JM, Kwiatkowski AV, Yang C, Korobova F, Pokutta S, Svitkina T, Weis WI, Nelson WJ (2010). AlphaE-catenin regulates actin dynamics independently of cadherin-mediated cell-cell adhesion. J Cell Biol 189, 339–352.
Bhunia AK, Piontek K, Boletta A, Liu L, Qian F, Xu PN, Germino FJ, Germino GG (2002). PKD1 induces p21(waf1) and regulation of the cell cycle via direct activation of the JAK-STAT signaling pathway in a process requiring PKD2. Cell 109, 157–168.
Blaschke S, Mueller CA, Markovic-Lipkovski J, Puch S, Miosge N, Becker V, Mueller GA, Klein G (2002). Expression of cadherin-8 in renal cell carcinoma and fetal kidney. Int J Cancer 101, 327–334.
Boca M, Distefano G, Qian F, Bhunia AK, Germino GG, Boletta A (2006). Polycystin-1 induces resistance to apoptosis through the phosphatidylinositol 3-kinase/Akt signaling pathway. J Am Soc Nephrol 17, 637–647.
Brunner FP, Rector FC, Seldin DW (1966). Mechanism of glomerulotubular balance. II. Regulation of proximal tubular reabsorption by tubular volume, as studied by stopped-flow microperfusion. J Clin Invest 45, 603–611.
Calvet JP (1993). Polycystic kidney disease: primary extracellular matrix abnormality or defective cellular differentiation? Kidney Int 43, 101–108.
Chapin HC, Caplan MJ (2010). The cell biology of polycystic kidney disease. J Cell Biol 191, 701–710.
Charron AJ, Bacallao RL, Wandinger-Ness A (2000a). ADPKD: a human disease altering Golgi function and basolateral exocytosis in renal epithelia. Traffic 1, 675–686.
Charron AJ, Nakamura S, Bacallao R, Wandinger-Ness A (2000b). Compromised cytoarchitecture and polarized trafficking in autosomal dominant polycystic kidney disease cells. J Cell Biol 149, 111–124.
Dias AS, de Almeida I, Belmonte JM, Glazier JA, Stern CD (2014). Somites without a clock. Science 343, 791–795.
Ehrlich JS, Hansen MD, Nelson WJ (2002). Spatio-temporal regulation of Rac1 localization and lamellipodia dynamics during epithelial cell-cell adhesion. Dev Cell 3, 259–270.
Engelberg JA, Datta A, Mostov KE, Hunt CA (2011). MDCK cystogenesis driven by cell stabilization within computational analogues. PLoS Comput Biol 7, e1002030.
Fedeles SV, Gallagher AR, Somlo S (2014). Polycystin-1: a master regulator of intersecting cystic pathways. Trends Mol Med 20, 251–260.
Fischer E, Legue E, Doyen A, Nato F, Nicolas J-F, Torres V, Yaniv M, Pontoglio M (2006). Defective planar cell polarity in polycystic kidney disease. Nat Genet 38, 21–23.
Gallagher AR, Hidaka S, Gretz N, Witzgall R (2002). Molecular basis of autosomal-dominant polycystic kidney disease. Cell Mol Life Sci 59, 682–693.
Gin E, Tanaka EM, Brusch L (2010). A model for cyst lumen expansion and size regulation via fluid secretion. J Theor Biol 264, 1077–1088.
Glazier JA, Graner F (1993). Simulation of the differential adhesion driven rearrangement of biological cells. Phys Rev E Stat Phys Plasmas Fluids Relat Interdiscip Topics 47, 2128–2154.
Gunay-Aygun M (2009). Liver and kidney disease in ciliopathies. Am J Med Genet C Semin Med Genet 151C, 296–306.
Hardy S, Kitamura M, Harris-Stansil T, Dai Y, Phipps ML (1997). Construction of adenovirus vectors through Cre-lox recombination. J Virol 71, 1842–1849.
Harris PC, Torres VE (2009). Polycystic kidney disease. Annu Rev Med 60, 321–337.
Harris PC, Torres VE (2014). Genetic mechanisms and signaling pathways in autosomal dominant polycystic kidney disease. J Clin Invest 124, 2315–2324.
Herbert BS, Grimes BR, Xu WM, Werner M, Ward C, Rossetti S, Harris P, Bello-Reuss E, Ward HH, Miller C, *et al.* (2013). A telomerase immortalized human proximal tubule cell line with a truncation mutation (Q4004X) in polycystin-1. PLoS One 8, e55191.
Kathem SH, Mohieldin AM, Nauli SM (2014). The roles of primary cilia in polycystic kidney disease. AIMS Mol Sci 1, 27–46.
Katsamba P, Carroll K, Ahlsen G, Bahna F, Vendome J, Posy S, Rajebhosale M, Price S, Jessell TM, Ben-Shaul A, *et al.* (2009). Linking molecular affinity and cellular specificity in cadherin-mediated adhesion. Proc Natl Acad Sci USA 106, 11594–11599.
Kher R, Sha EC, Escobar MR, Andreoli EM, Wang P, Xu WM, Wandinger-Ness A, Bacallao RL (2011). Ectopic expression of cadherin 8 is sufficient to cause cyst formation in a novel 3D collagen matrix renal tubule culture. Am J Physiol Cell Physiol 301, C99–C105.
Kim JB, Islam S, Kim YJ, Prudoff RS, Sass KM, Wheelock MJ, Johnson KR (2000). N-Cadherin extracellular repeat 4 mediates epithelial to mesenchymal transition and increased motility. J Cell Biol 151, 1193–1206.
Koulen P, Cai Y, Geng L, Maeda Y, Nishimura S, Witzgall R, Ehrlich BE, Somlo S (2002). Polycystin-2 is an intracellular calcium release channel. [see comment]. Nat Cell Biol 4, 191–197.
Koulen P, Duncan RS, Liu J, Cohen NE, Yannazzo J-AS, McClung N, Lockhart CL, Branden M, Buechner M (2005). Polycystin-2 accelerates Ca2+ release from intracellular stores in Caenorhabditis elegans. Cell Calcium 37, 593–601.
Kücken M, Soriano J, Pullarkat PA, Ott A, Nicola EM (2008). An osmoregulatory basis for shape oscillations in regenerating hydra. Biophys J 95, 978–985.
Lanoix J, D'Agati V, Szabolcs M, Trudel M (1996). Dysregulation of cellular proliferation and apoptosis mediates human autosomal dominant polycystic kidney disease (ADPKD). Oncogene 13, 1153–1160.
Li X, Luo Y, Starremans PG, McNamara CA, Pei Y, Zhou J (2005). Polycystin-1 and polycystin-2 regulate the cell cycle through the helix-loop-helix inhibitor Id2. Nat Cell Biol 7, 1202–1212 [correction published in Nat Cell Biol (2006), 8,100].
Magno R, Grieneisen VA, Marée AF (2015). The biophysical nature of cells: potential cell behaviours revealed by analytical and computational studies of cell surface mechanics. BMC Biophys 8, 8.
Manzati E, Aguiari G, Banzi M, Manzati M, Selvatici R, Falzarano S, Maestri I, Pinton P, Rizzuto R, del Senno L (2005). The cytoplasmic C-terminus of polycystin-1 increases cell proliferation in kidney epithelial cells through serum-activated and Ca(2+)-dependent pathway(s). Exp Cell Res 304, 391–406.
Markoff A, Bogdanova N, Knop M, Ruffer C, Kenis H, Lux P, Reutelingsperger C, Todorov V, Dworniczak B, Horst J, *et al.* (2007). Annexin A5 interacts with polycystin-1 and interferes with the polycystin-1 stimulated recruitment of E-cadherin into adherens junctions. J Mol Biol 369, 954–966.
Martz E, Steinberg MS (1972). The role of cell-cell contact in "contact" inhibition of cell division: a review and new evidence. J Cell Physiol 79, 189–210.
McNeill H (2009). Planar cell polarity and the kidney. J Am Soc Nephrol 20, 2104–2111.
Mekahli D, Parys JB, Bultynck G, Missiaen L, De Smedt H (2013). Polycystins and cellular Ca2+ signaling. Cell Mol Life Sci 70, 2697–2712.
Menezes LF, Cai Y, Nagasawa Y, Silva AM, Watkins ML, Da Silva AM, Somlo S, Guay-Woodford LM, Germino GG, Onuchic LF, *et al.* (2004). Polyductin, the PKHD1 gene product, comprises isoforms expressed in plasma membrane, primary cilium, and cytoplasm. Kidney Int 66, 1345–1355.
Nadasdy T, Laszik Z, Blick KE, Johnson DL, Burst-Singer K, Nast C, Cohen AH, Ormos J, Silva FG (1995a). Human acute tubular necrosis: a lectin and immunohistochemical study. Hum Pathol 26, 230–239.
Nadasdy T, Laszik Z, Blick KE, Johnson LD, Silva FG (1994). Proliferative activity of intrinsic cell populations in the normal human kidney. J Am Soc Nephrol 4, 2032–2039.
Nadasdy T, Laszik Z, Lajoie G, Blick KE, Wheeler DE, Silva FG (1995b). Proliferative activity of cyst epithelium in human renal cystic diseases. J Am Soc Nephrol 5, 1462–1468.
Nakajima Y, Meyer EJ, Kroesen A, McKinney SA, Gibson MC (2013). Epithelial junctions maintain tissue architecture by directing planar spindle orientation. Nature 500, 359–362.
Park JY, Schutzer WE, Lindsley JN, Bagby SP, Oyama TT, Anderson S, Weiss RH (2007). p21 is decreased in polycystic kidney disease and leads to increased epithelial cell cycle progression: roscovitine augments p21 levels. BMC Nephrol 8, 12.
Popławski NJ, Shirinifard A, Swat M, Glazier JA (2008). Simulation of single-species bacterial-biofilm growth using the Glazier-Graner-Hogeweg model and the CompuCell3D modeling environment. Math Biosci Eng 5, 355–388.
Rivers RL, McAteer JA, Clendenon JL, Connors BA, Evan AP, Williams JC (1996). Apical membrane permeability of MDCK cells. Am J Physiol 271, C226–C234.
Rohatgi R, Battini L, Kim P, Israeli S, Wilson PD, Gusella GL, Satlin LM, Rohatgi R, Battini L, Kim P, *et al.* (2008). Mechanoregulation of intracellular Ca2 +in human autosomal recessive polycystic kidney disease cyst-lining renal epithelial cells. Am J Physiol Renal Physiol 294, F890–F899.
Roignot J, Peng X, Mostov K (2013). Polarity in mammalian epithelial morphogenesis. Cold Spring Harb Perspect Biol 5, a013789.
Roitbak T, Ward CJ, Harris PC, Bacallao R, Ness SA, Wandinger-Ness A (2004). A polycystin-1 multiprotein complex is disrupted in polycystic kidney disease cells. Mol Biol Cell 15, 1334–1346.

Schindelin J, Arganda-Carreras I, Frise E, Kaynig V, Longair M, Pietzsch T, Preibisch S, Rueden C, Saalfeld S, Schmid B, *et al*. (2012). Fiji: an open source platform for biological-image analysis. Nat Methods 9, 676–682.
Scianna M, Munaron L, Preziosi L (2011). A multiscale hybrid approach for vasculogenesis and related potential blocking therapies. Prog Biophys Mol Biol 106, 450–462.
Sharma N, Malarkey EB, Berbari NF, O'Connor AK, Vanden Heuvel GB, Mrug M, Yoder BK (2013). Proximal tubule proliferation is insufficient to induce rapid cyst formation after cilia disruption. J Am Soc Nephrol 24, 456–464.
Silberberg M, Charron AJ, Bacallao R, Wandinger-Ness A (2005). Mispolarization of desmosomal proteins and altered intercellular adhesion in autosomal dominant polycystic kidney disease. Am J Physiol Renal Physiol 288, F1153–F1163.
Starruß J, Bley T, Søgaard-Andersen L, Deutsch A (2007). A new mechanism for collective migration in Myxococcus xanthus. J Stat Phys 128, 269–286.
Stayner C, Zhou J (2001). Polycystin channels and kidney disease. Trends Pharmacol Sci 22, 543–546.
Swat MH, Hester SD, Balter AI, Heiland RW, Zaitlen BL, Glazier JA (2009). Multicell simulations of development and disease using the CompuCell3D simulation environment. Methods Mol Biol 500, 361–428.
Swat MH, Thomas GL, Belmonte JM, Shirinifard A, Hmeljak D, Glazier JA (2012). Multi-scale modeling of tissues using CompuCell3D. Methods Cell Biol 110, 325–366.
Thiery JP, Engl W, Viasnoff V, Dufour S (2012). Biochemical and biophysical origins of cadherin selectivity and adhesion strength. Curr Opin Cell Biol 24, 614–619.
Torres VE, Harris PC (2009). Autosomal dominant polycystic kidney disease: the last 3 years. Kidney Int 76, 149–168.
van Adelsberg J (2000). Polycystin-1 interacts with E-cadherin and the catenins—clues to the pathogenesis of cyst formation in ADPKD? Nephrol Dial Transplant 15, 1–2.
Vassilev PM, Guo L, Chen XZ, Segal Y, Peng JB, Basora N, Babakhanlou H, Cruger G, Kanazirska M, Ye C, *et al*. (2001). Polycystin-2 is a novel cation channel implicated in defective intracellular Ca(2+) homeostasis in polycystic kidney disease. Biochem Biophys Res Commun 282, 341–350.
Wheelock MJ, Shintani Y, Maeda M, Fukumoto Y, Johnson KR (2008). Cadherin switching. J Cell Sci 121, 727–735.
Wilson PD (2004). Polycystic kidney disease: new understanding in the pathogenesis. Int J Biochem Cell Biol 36, 1868–1873.
Wilson P, Schrier R, Breckon R, Gabow P (1986). A new method for studying human polycystic kidney disease epithelia in culture. Kidney Int 30, 371–378.
Yamaguchi T, Wallace DP, Magenheimer BS, Hempson SJ, Grantham JJ, Calvet JP (2004). Calcium restriction allows cAMP activation of the B-Raf/ERK pathway, switching cells to a cAMP-dependent growth-stimulated phenotype. J Biol Chem 279, 40419–40430.